Supplement of Atmos. Chem. Phys., 25, 9669–9684, 2025
https://doi.org/10.5194/acp-25-9669-2025-supplement

Atmospheric Chemistry and Physics
Open Access

Supplement of

The 21st-century wetting inhibits growing surface ozone in Northwestern China

Xiaodong Zhang et al.

Correspondence to: Xiaodong Zhang (zhangxd2020@pku.edu.cn) and Hong Gao (honggao@lzu.edu.cn)

S1. WRF-Chem configuration

WRF-Chem V3.7 provides multiple choices for physics parameterization and atmospheric chemistry to supports different solution schemes for different modeling scenario simulations. Of which, WRF provides meteorology, including winds, air temperature, humidity turbulent diffusion and dispersion, atmospheric radiation, and clouds evolution, to drive O_3 chemical transformation, transport, and mixing in the atmosphere (https://www2.acom.ucar.edu/wrf-chem). The physical parameterization and chemistry schemes chosen in the present study and the model vertical levels are presented in Tables S1 and S2. The Regional Acid Deposition Model version 2 (RADM2) and the MADE/SORGAM aerosol modules were adopted in chemistry and aerosol simulations (Ackermann et al., 1998; Stockwell et al., 1990; Zhou et al., 2017). The FAST-J photolysis scheme was used to calculate photolysis rates for complex photochemical reactions, accounting for the intricate interplay between atmospheric particulates and solar irradiance (Chen and Dudhia, 2001). The modeling adopted a robust array of physical schemes, including the Noah land surface model (Schell et al., 2001), the Mellor-Yamada-Janjic (MYJ) boundary layer scheme (Janjić, 1994), the Grell-Devenyi ensemble convective parameterization (Grell and Dévényi, 2002), the Lin microphysics scheme, the Goddard shortwave radiation scheme (Lin et al., 1983), and the Rapid Radiative Transfer Model (RTTM) for longwave radiation (Chou et al., 1998). These schemes have been used in extensive WRF-Chem simulations of tropospheric O_3 activities in China and demonstrated to be reliable in O_3 modeling exercises (Jiang et al., 2008, 2012; Li et al., 2020; Xiang et al., 2020; Zhang et al., 2020, 2022). The aerosol feedback mechanism was also considered to account for the interactions between aerosols and solar radiation, leading to potentially more accurate simulations of atmospheric processes.

The model input emissions include gridded annual emission data for BC, OC, NH_3, NMVOC, NOx, CO, SO_2, and primary PM_{10} and $PM_{2.5}$ at a resolution of 0.1° × 0.1° lat/lon, collected from the EDGAR version 4.3 (The Emissions Database for Global Atmospheric Research). A simple grid-mapping program was used to process EDGAR's data (https://ruc.noaa.gov/wrf/wrf-chem/Emission_guide.pdf). The program maps the global anthropogenic emissions data to the WRF-forecasting domain using a Mercator, polar stereographic or Lambert conformal projection. It is worth noting that a recent study suggests that temperature can alter precursor emissions, thereby influencing ozone formation in some regions (Pfannerstill et al., 2024). Unfortunately, the present study is not able to identify the impacts of humidification and warming on precursor emissions because we implemented available well-known precursor emission inventories, such as MEIC and EDGAR, into the WRF-Chem model. To account for

the influences of humidity and temperature on precursor emissions, regional or global emission inventories have to be dynamically updated based on altering humidity and temperature in future.

The model domain covers entire mainland China and is not nested because this model study focused on a national scale. The model was integrated during each summer (June, July, and August) from 1998 to 2017. In the WRF-Chem model, the stratosphere-troposphere exchange (STE) parameterization is typically included as part of the model's default configuration. This means that the model is designed to automatically account for the exchange of ozone between the stratosphere and troposphere through the STE process. To account for the annual cycle of summer meteorology and chemical equilibrium, three-days spin-up time is selected for every summer. We did not use any data assimilation techniques in O_3 simulations because the model integration was repeated on a daily basis with daily initial condition input. However, the nudging option (FDDA) in WRF simulations was switched in our modeling exercises to avoid the drift of meteorology from the global reanalysis.

S2. Model evaluation

Extensive model evaluations were conducted by comparing simulated ozone concentrations, with measured data. The CNEMC (China National Environmental Monitoring Center, https://air.cnemc.cn:18007/) datasets were used for modeled O_3 evaluation. The CNEMC provided monitored hourly near-surface ozone concentrations since 2013 across China but the CNEMC air quality data were most reliable since 2016. The selected eight validation cities' latitudes and longitudes are shown in Table S3. Figures S2-S7 shows modeled and sampled hourly O_3 concentrations during the period of summer 2019 under SSP2-4.5 and SSP5-8.5 scenarios, respectively. Modeled O_3 concentrations capture, to some extent, the fluctuations of sampled concentrations with the correlation coefficients >0.55. For the evaluation of modeled meteorology, readers are referred to refs. Zhang et al. (2020 and 2022). It should be noted that simulated O_3 concentrations in Northwestern China do not match well compared to eastern China. Likely higher background O_3 concentrations in Northwestern China than Eastern China due to topography, featured by mountainous regions and plateaus that can influence local atmospheric circulation patterns and the trapping of pollutants, stronger sunshine, scarce precursor emission sources, and dry condition. WRF model often could not predict well meteorology in complex terrains.

S3. Shared socioeconomic pathway in conjunction with representative concentration pathways from 2019 to 2060

First, we selected the CMIP6 SSP2-RCP4.5 pathway, which reflects a middle-of-the-road pathway regarding socioeconomic factors (SSP2) and a moderate level of efforts to combat climate change. RCP4.5 is a stabilization scenario where the increase in radiative forcing is stabilized shortly after 2100 through various technologies and strategies for reducing greenhouse gas emissions. The SSP2-RCP4.5 (hereafter referred to as SSP2-4.5) is the pathway that reasonably approximates the strategies to achieve GHG emission mitigation goals in Northwestern China. Under SSP2-4.5, the growth in the duration and intensity of droughts tends to be slow and steady (Zhou et al., 2023; Zhu et al., 2020). Meteorology and precursor emissions subject to SSP2-4.5 in China were collected from the DPEC in 2019, 2030, and 2060, respectively. To compare, we also performed model simulations subject to the SSP5-RCP8.5 scenario (hereafter referred to as SSP5-8.5). The SSP5-RCP8.5 represents a scenario where socioeconomic trends focus on economic growth reliant on fossil fuels without significant efforts to mitigate climate change, leading to high greenhouse gas emissions and substantial global warming by the end of the 21st century. This scenario projects a higher drought risk than other SSP-RCP pathways (Nooni et al., 2021; Zhu et al., 2020). Like the SSP2-RCP4.5 scenario setup, the meteorology and precursor emissions subject to SSP5-8.5 in 2019, 2030, and 2060 were also collected from the DPEC.

S4. Projected future climate impacts on summer Ozone

Figure 6 illustrates WRF-Chem modeled fractions of gridded O_3 concentration and RH of 2030 and 2060 to 2019 under SSP2-4.5 scenario (Fig. 6a-6d) in Northwestern and mainland China (the left-low corner of Fig. 6), respectively. The results show a widespread decline in O_3 concentrations from 2019 to 2030 in Northwestern China. Most areas in mainland China featured negative O_3 fractions, except for Xinjiang and Eastern Inner Mongolia (Fig. 6a). However, O_3 concentrations in those southern provinces of Northwestern China, namely Eastern Qinghai, Eastern Gansu, and Shaanxi, will rise in 2060 relative to 2019 (Fig. 6b), which is consistent with widespread enhancement of O_3 levels in Central and Eastern China (inner figure on the low-left corner). Opposite to the wetting during the past two decades (Figs. 2 and 3 in main text), we observe a drying trend extending from Xinjiang to Western Gansu and Qinghai, illustrated by negative RH fractions in 2030 and 2060 relative to 2019 (Figs. 6c and 6d). The drying trend seems, to some extent, consistent with increasing O_3 concentrations in Xinjiang. Although we can also observe negative associations between O_3 and RH, such as in Ningxia, Shaanxi, and Inn Mongolia from 2019 to 2030, such negative associations are not applicable in many places of Northwestern and mainland China subject to the SSP2-4.5 scenario, particularly in 2060. This can be attributed to strong

artificial interventions in O_3 mitigation in China since the early 2020s (https://www.gov.cn/zhengce/content/2022-01/24/content_5670202.htm), typically in Eastern, Southern, and Central China. Since SSP2-4.5 projects a moderate development pathway where trends do not shift markedly from historical patterns, artificial interventions may overwhelm natural climate factors' influences on O_3 evolution. The strong signals in RH and O_3 associations were identified before the artificial interventions were implemented, as discussed in section 3.2.

Figure 6e compares modeled fractions of mean summer RH, SAT, and O_3 concentrations between 2030 and 2060 relative to 2019 under the SSP2-4.5 scenario averaged over each of the six provinces in Northwestern China. SAT (green bars) in all six provinces tends to decline from 2019, as shown by the negative SAT fractions, ranging from -2.9% in Inner Mongolia to -12.2% in Qinghai. Declining O_3 levels seem to correspond to falling SATs in Ningxia (-12.9%), Shaanxi (-10.3%), Gansu (-8.8%), and Qinghai (-3.8%) but not in Xinjiang and Inner Mongolia, where declining SATs align with growing O_3 levels. Detailed data can be found in Table S7. Among the six provinces, RH (yellow bars) tends to incline in Ningxia by 10.8% from 2019 to 2030, during which mean O_3 concentration reduces about 13%, but decline in rest of five provinces with most significant drop in Xinjiang by -47.8% in 2030, which accompanies with a weak increase of O_3 level, featured by the positive O_3 fraction. By 2060, RH and SAT fractions between 2019 and 2060 show identical fluctuations as those between 2019 and 2030 but differ in magnitudes. However, O_3 fractions illustrate opposite fluctuations compared to 2030, turning from negative to positive in Ningxia, Shaanxi, Gansu, and Qinghai, suggesting that growing O_3 concentrations in 2060 relative to 2019 and 2030, respectively. The negative correlations between O_3 and RH fractions occur in Shaanxi, Gansu and Qinghai. Overall, the changes in O_3 concentrations subject to SSP2-4.5 are not markedly associated with RH variations. The results can be partly attributed to O_3 mitigation campaigns and strategies from the late 2010s (http://english.craes.cn/), aiming to reduce and eliminate O_3 precursor emissions effectively. These anthropogenic activities overwhelmed the climate effect on the O_3 trend, so we did not discern good associations of O_3 concentrations with STA and RH (Fig. 6).

The SSP5-8.5 scenario projects the most robust warming trends among all SSP-RCP scenarios in China, resulting in different patterns in the fractions of O_3 concentrations and RH in Northwestern China from 2019 to 2030 (Fig. 7a and 7c), showing a wetting trend extending from Xinjiang, western Gansu, to entire Inn Mongolia (positive RH fractions, Fig. 7c). Accordingly, we observe negative O_3 fraction in these regions, indicating falling O_3 levels from 2019 to 2030 (Fig. 7a). We can also discern growing O_3 concentrations (positive O_3 fractions) in the southern part

of Northwestern China across Qinghai, Eastern Gansu, and Shaanxi (Fig. 7a), corresponding to decreasing RH, featured by negative RH fractions (Fig. 7c). In the next three decades to 2060, the negative associations between O_3 and RH fractions still remain in the northern part of Northwestern China, but O_3 concentrations in the southern part of Northwestern China during 2019 to 2060 will decline (negative O_3 fractions, Fig. 7b), corresponding to increasing RH (positive fraction, Fig. 7d). The good associations between O_3 and RH fractions suggest that, given strong climate fluctuations projected by the SSP5-8.5, the artificial interventions play a weaker role in O_3 evolution than SSP2-4.5.

Significant differences between the SAT, RH, and O_3 fractions of 2030 and 2060 to 2019 (Table S8 and Fig. 7e), subject to SSP5-8.5 from SSP2-4.5 (Fig. 6e), can be readily identified. SAT fractions become very small and less than ±5%, though fluctuating positively (meaning warming) and negatively (indicating cooling), in most provinces (inner figure on the central bottom of Fig. 7e), implying weak changes in SAT or climate in Northwestern China. From 2019 to 2030, Inner Mongolia, Gansu, and Xinjiang will experience wetting with growing positive RH fractions ranging from 9.0% (Gansu) to 34.9% (Xinjiang). Accordingly, we can observe falling O_3 levels characterized by their negative fractions, though not very significant (Fig. 7e), except for Gansu. For the next three decades to 2060, RH fractions in these three provinces turn to negative, suggesting drying, corresponding to increasing O_3 (positive fraction), except for Gansu. The RH fractions from 2019 to 2030 and 2060 in the other three provinces (Shaanxi, Ningxia, and Qinghai) are also opposite, showing the transition of drying (negative fractions) from 2019 to 2030 to wetting (positive fraction) from 2019 to 2060. These results indicate that the northern part of Northwestern China will become further humidified by 2030 relative to 2019. Meanwhile, the southern part will experience a transition from drying to wetting from 2030 to 2060, corresponding to declining O_3 levels.

Modeled RH (%) and SAT(C^o) summer month time series under SSP2-4.5 and SSP 5-8.5 scenarios in 2019, 2030, and 2060 over Northwestern China are illustrated in Fig. S15.

Table S1. Physical and chemical parametrization scheme used in WRF-Chem model

	WRF-Chem
microphysics scheme	Lin
shortwave radiation scheme	Goddard
longwave radiation scheme	RRTM
surface layer scheme	MYJ
boundary layer scheme	MYJ TKE
cumulus scheme	Grell-3
photolysis scheme	Fast-J
chemical mechanisms	RADM2
aerosols module	MADE/SORGAM

Table S2. The eta levels and corresponding heights above the sea level of WRF-Chem model setup.

layer	**eta-value**	**Height(m)**	**layer**	**eta-value**	**Height(m)**
1	0.000	20580	16	0.493	4368
2	0.015	19019	17	0.566	3437
3	0.026	17995	18	0.645	2441
4	0.040	15948	19	0.711	1370
5	0.057	14924	20	0.760	1020
6	0.076	13899	21	0.808	757
7	0.098	12879	22	0.856	568
8	0.125	11880	23	0.895	405
9	0.154	10918	24	0.921	268
10	0.189	9973	25	0.944	157
11	0.226	9033	26	0.962	125
12	0.269	8096	27	0.977	95
13	0.317	7162	28	0.988	62
14	0.370	6230	29	0.997	32
15	0.428	5298	30	0.998	5

Table S3. The Location of eight cities in Figures S2-S4

Cite	longitude	latitude
Tongchuan	108.9°E-109.1°E	34.9°N-35.1°N
Shizuishan	106.3°E-106.5°E°	38.9°N-39.1°N
Turpan	89.2°E-90.1°E	43.0°N-43.9°N
Lanzhou	103.5°E-104.3°E	35.4°N-36.1°N
Karamay	84.9°E-85.1°E	45.5°N-45.7°N
Changchun	125.0°E-126.7°E	43.5°N-44.1°N
Jinan	116.9°E-117.9°E	36.4°N-37.4°N
Zhengzhou	113.3°E-113.8°E	34.5°N-34.9°N

Table S4. Statistics MRM prediction of O_3 concentration in Gansu

Linear Regression Analysis Results n=60									
	Unstandardized Coefficients		Standardized Coefficients	t	P	VIF	R^2	Adjusted R^2	F
	B	Standard Error	Beta						
Constant	15.554	4.883	-	3.185	0.002***	-			
lnRH	-0.089	0.047	-0.236	-1.913	0.061*	-1.009	0.143	0.113	F=4.762 P=0.012**
lnSAT	-1.92	0.859	-0.275	-2.234	0.029**	1.009			
Dependent Variable: lnO_3									

Note: ***, **, and * indicate significance levels of 1%, 5%, and 10%.

Table S5. Statistics MRM prediction of O_3 concentration in Xinjiang

Linear Regression Analysis Results n=60									
	Unstandardized Coefficients		Standardized Coefficients	t	P	VIF	R^2	Adjusted R^2	F
	B	Standard Error	Beta						
Constant	11.324	1.977	-	5.728	0.000***	-			
lnRH	-1.148	0.346	-0.257	-3.316	0.002***	1.130	0.696	0.686	F=65.367 P=0.000***
lnSAT	-0.16	0.014	-0.886	-11.419	0.029**	1.009			
Dependent Variable: lnO_3									

Note: ***, **, and * indicate significance levels of 1%, 5%, and 10%.

Table S6. Statistics MRM prediction of O_3 concentration in Qinghai

Linear Regression Analysis Results n=60									
	Unstandardized Coefficients		Standardized Coefficients	t	P	VIF	R^2	Adjusted R^2	F
	B	Standard Error	Beta						
Constant	-24.482	9.028	-	-2.712	0.009***	-			
lnRH	5.373	1.582	0.343	3.397	0.001***	1.15	0.493	0.476	F=27.762 P=0.000***
lnSAT	-0.38	0.077	-0.501	-4.957	0.000***	1.15			
Dependent Variable: lnO_3									

Note: ***, **, and * indicate significance levels of 1%, 5%, and 10%.

Table S7. Modeled fractions of mean summer RH, SAT, and O_3 concentrations between 2030 and 2060 relative to 2019 under the SSP2-4.5 scenario

	RH_{24530}(%)	RH_{24560}(%)	T_{24530}(%)	T_{24560}(%)	O_{3_24530}(%)	O_{3_24560}(%)
Inner Mongolia	-14.23	-10.42	-2.92	-3.24	4.72	-11.67
Ningxia	10.80	29.90	-5.53	-6.13	-12.87	5.22
Shaanxi	-6.36	-4.40	-4.02	-4.51	-10.32	11.00
Gansu	-14.98	-17.08	-6.54	-6.86	-8.77	0.42
Xinjiang	-47.82	-54.59	-5.30	-5.55	0.99	-4.64
Qinghai	-10.32	-5.56	-12.18	-12.53	-3.83	7.01

Note: 24530 means the fraction from 2019 to 2030 under the SSP2-4.5 scenario; 24560 means the fraction from 2019 to 2060 under the SSP2-4.5 scenario.

Table S8. Modeled fractions of mean summer RH, SAT, and O_3 concentrations between 2030 and 2060 relative to 2019 under the SSP5-8.5 scenario

	RH_{58530}(%)	RH_{58560}(%)	T_{58530}(%)	T_{58560}(%)	O_{3_58530}(%)	O_{3_58560}(%)
Inner Mongolia	11.44	-4.46	-0.55	0.10	21.87	11.44
Ningxia	-23.53	29.00	0.21	0.31	2.58	-23.53
Shaanxi	-7.28	20.11	0.14	0.39	-1.51	-7.28
Gansu	8.97	-2.55	-0.72	-0.15	-2.79	8.97
Xinjiang	34.92	-13.95	-0.50	0.03	2.72	34.92
Qinghai	-16.59	8.37	-0.50	-0.42	-0.20	-16.59

Note: 58530 means the fraction from 2019 to 2030 under the SSP5-8.5 scenario; 58560 means the fraction from 2019 to 2060 under the SSP5-8.5 scenario.

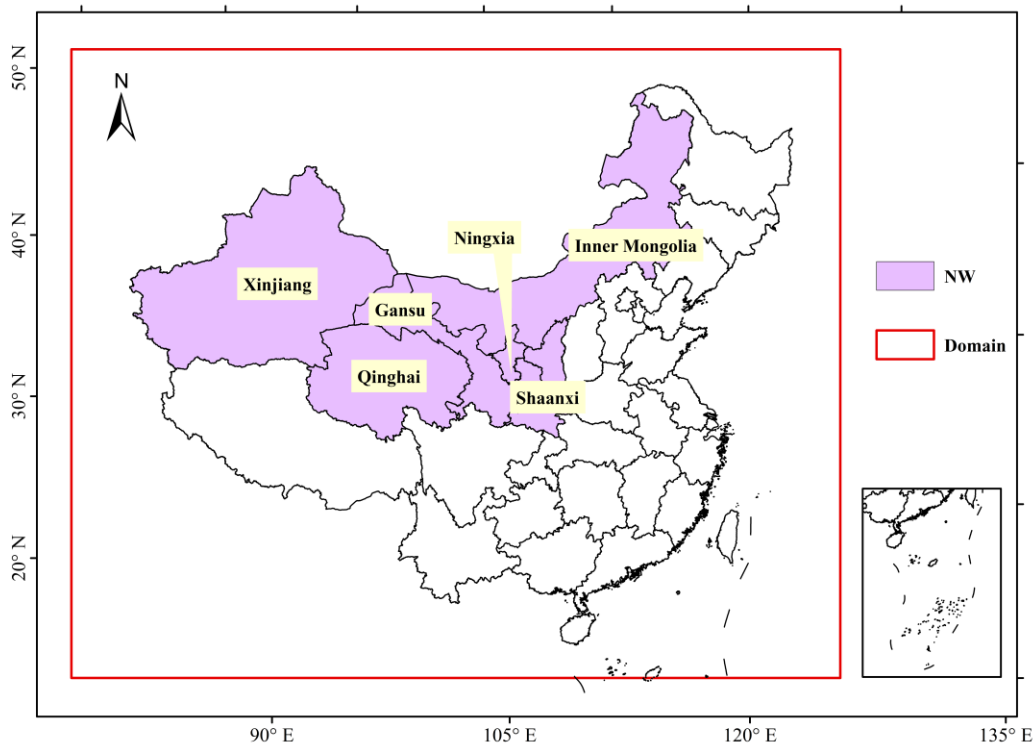

Fig. S1. Locations of six provinces in Northwest China (NW) and WRF-Chem domain (20 km resolution, red rectangle).

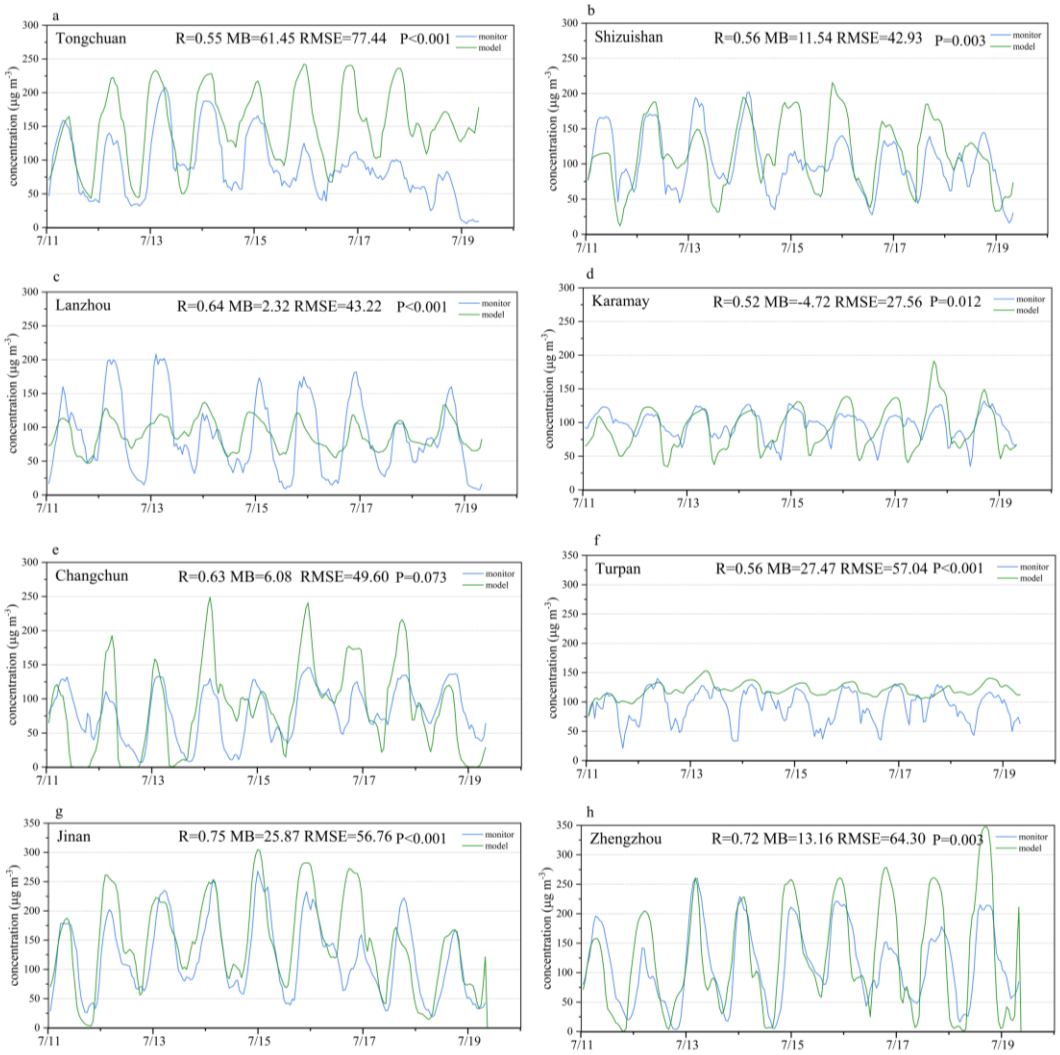

Fig. S2. Measured (solid blue line) and modeled (solid green line) ozone concentrations in eight cities in summer 2019 under SSP2-4.5 scenario. Correlation coefficient (R), mean bias (MB), root mean square errors (RMSE) and p-value are highlighted in each figure.

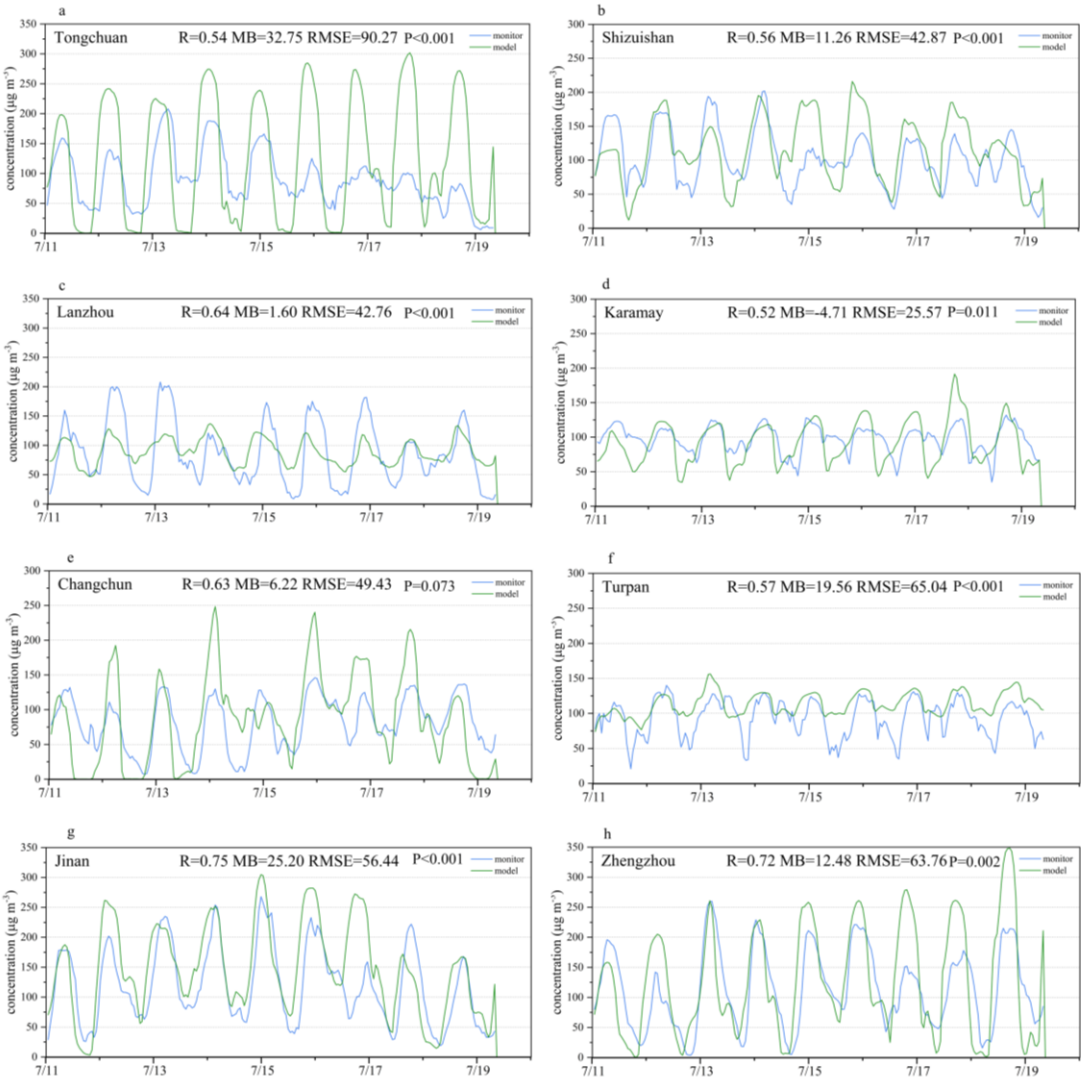

Fig. S3. Measured (solid blue line) and modeled (solid green line) ozone concentrations in eight cities in summer 2019 under SSP5-8.5 scenario. Correlation coefficient (R), mean bias (MB), root mean square errors (RMSE) and p-value are highlighted in each figure.

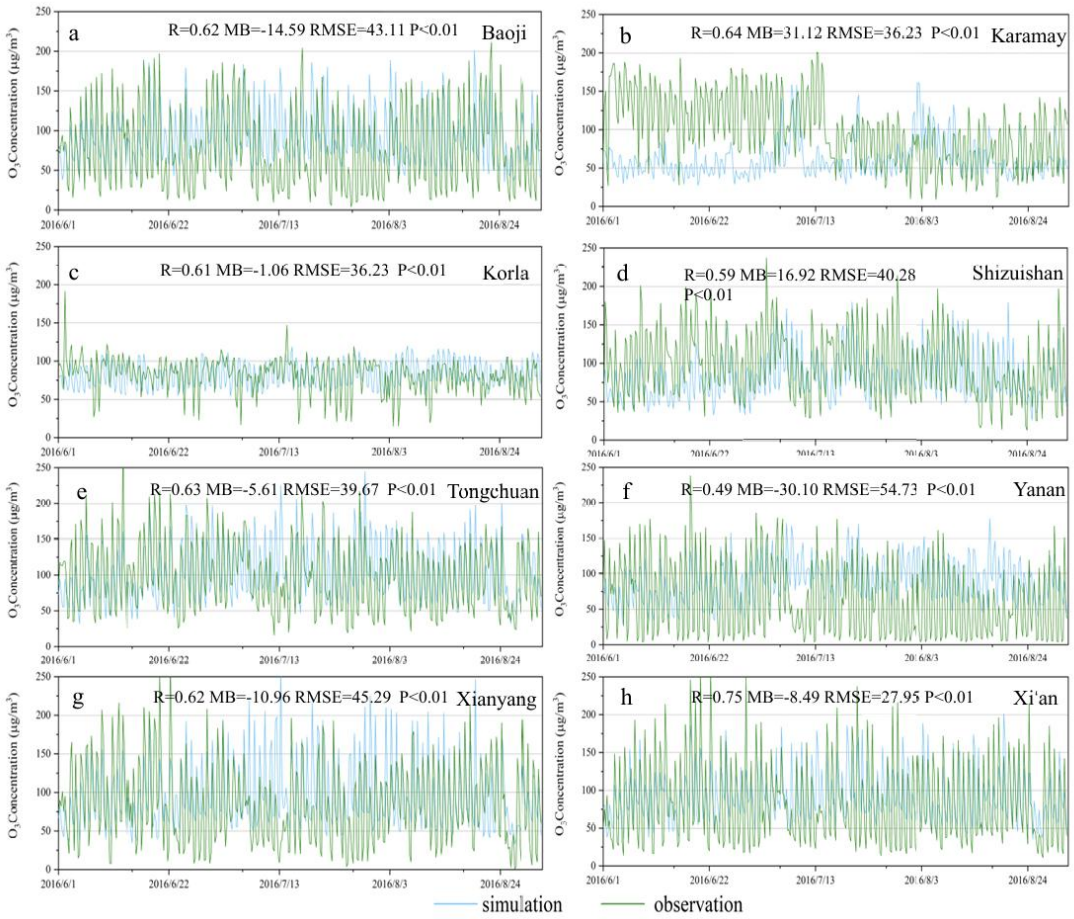

Fig. S4. Measured (solid blue line) and modeled (solid green line) ozone concentrations in eight cities in summer 2016. Correlation coefficient (R), mean bias (MB), root mean square errors (RMSE) and p-value are highlighted in each figure.

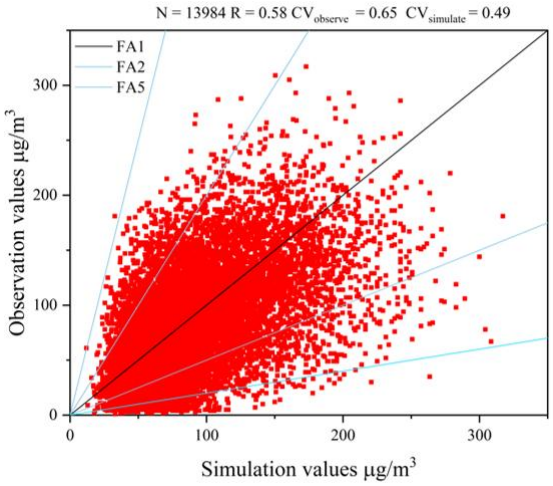

Fig. S5. A correlation diagram between modeled and measured six hourly (0200, 0800, 1400, S7 2000 LST) O_3 concentrations at the 38 CNEMC stations across China from June 1st to August 31st 2016. The number of total samples is 13984. R is correlation coefficient and CV is the coefficient of variation. FA1, FA2, and FA5 are the fractions of model values within factors of one to five of measure O_3 concentrations.

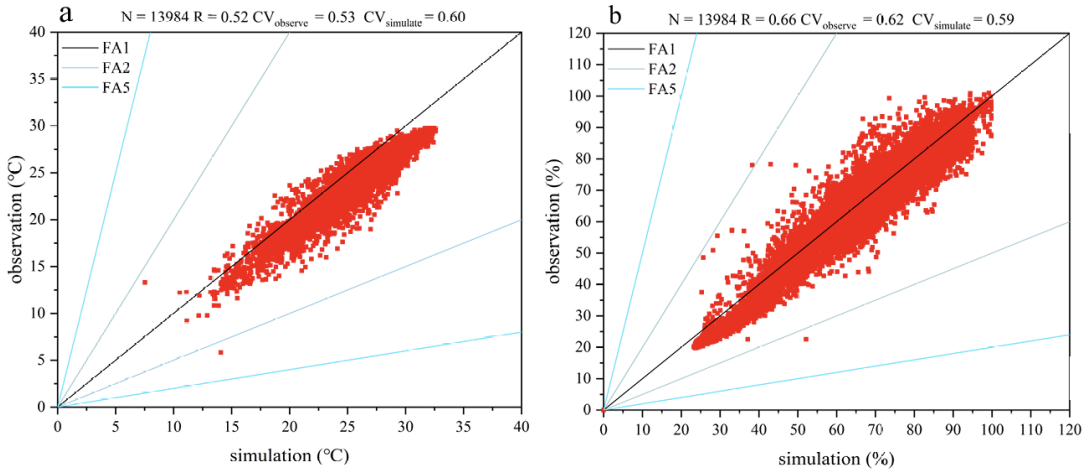

Fig. S6. A correlation diagram between modeled and measured six hourly (0200, 0800, 1400, S7 2000 LST) SAT (a) and RH (b) at the 38 CNEMC stations across China from June 1st to August 31st 2016. The number of total samples is 13984. R is correlation coefficient and CV is the coefficient of variation. FA1, FA2, and FA5 are fractions of model values within factors of one to five of measure values. SAT (a) and RH (b).

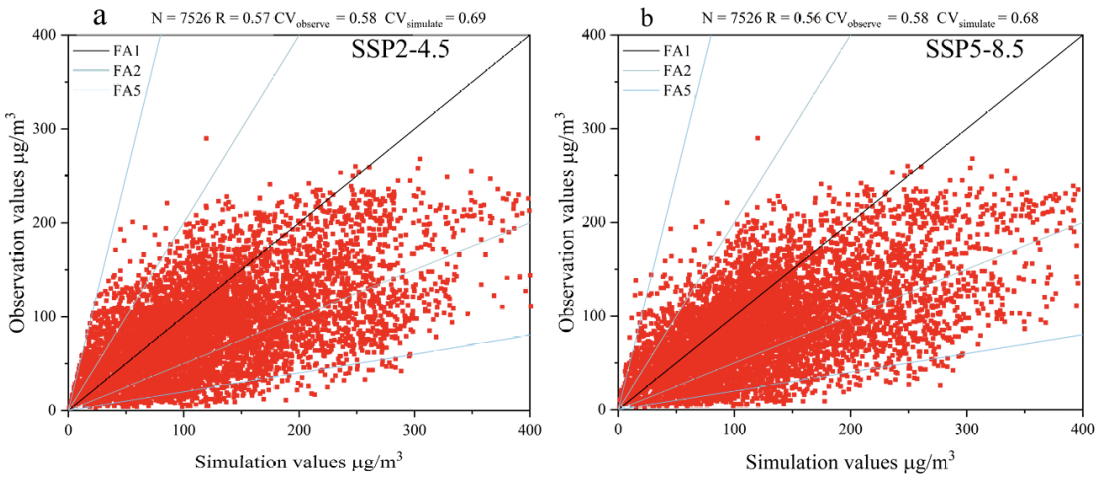

Fig. S7. A correlation diagram between modeled and measured hourly O_3 concentrations at the 38 CNEMC stations across China 2019. The number of total samples is 7526. R is correlation coefficient and CV is the coefficient of variation. FA1, FA2, and FA5 are the fractions of model values within factors of one to five of measure O_3 concentrations. (a) SSP2-4.5 scenario, (b) SSP5-8.5 scenario.

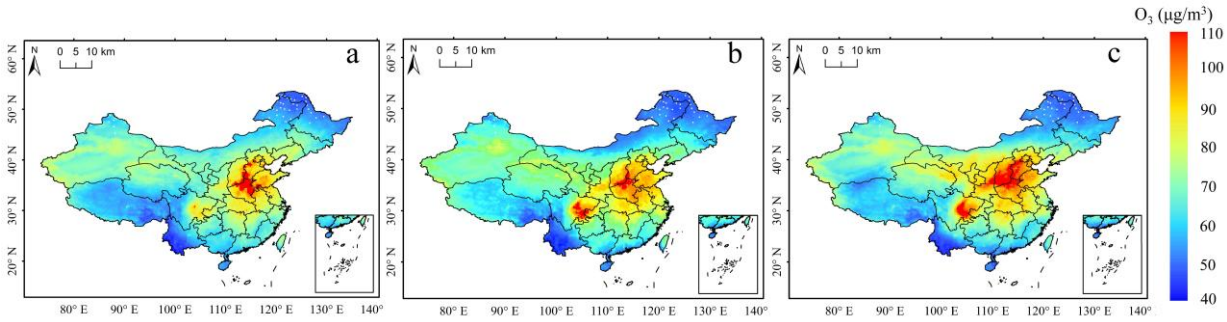

Fig. S8. WRF-Chem simulated O_3 concentration in 2004, (a) baseline scenario, (b) model S3 scenario (fixed meteorology in 1998), (c) fixed RH and SAT only in 1998.

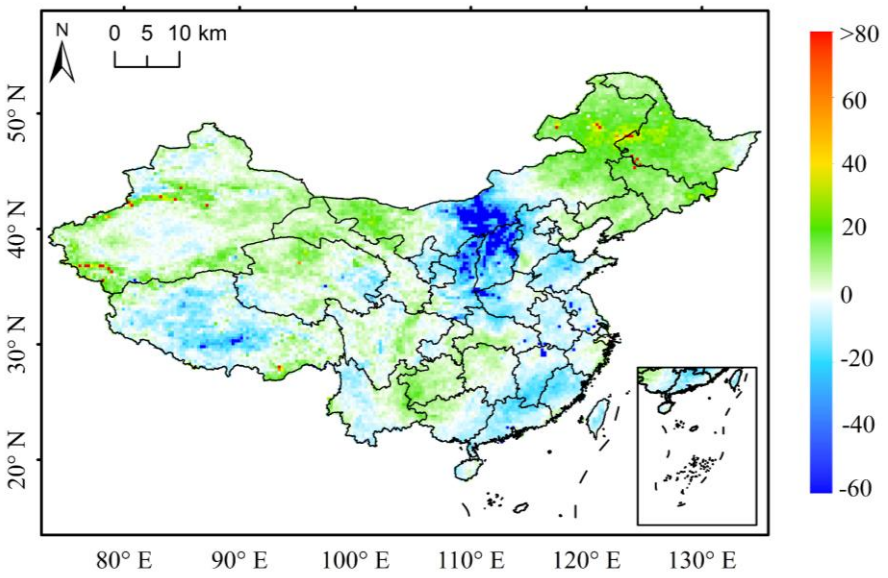

Fig. S9. Differences of planetary boundary layer height (PBLH, m) between model scenario 4 (fixed RH and SAT in 1998) and model scenario 3 (fixed meteorology in 1998), estimated by PBLH under scenario 4 minus PBLH under scenario 3.

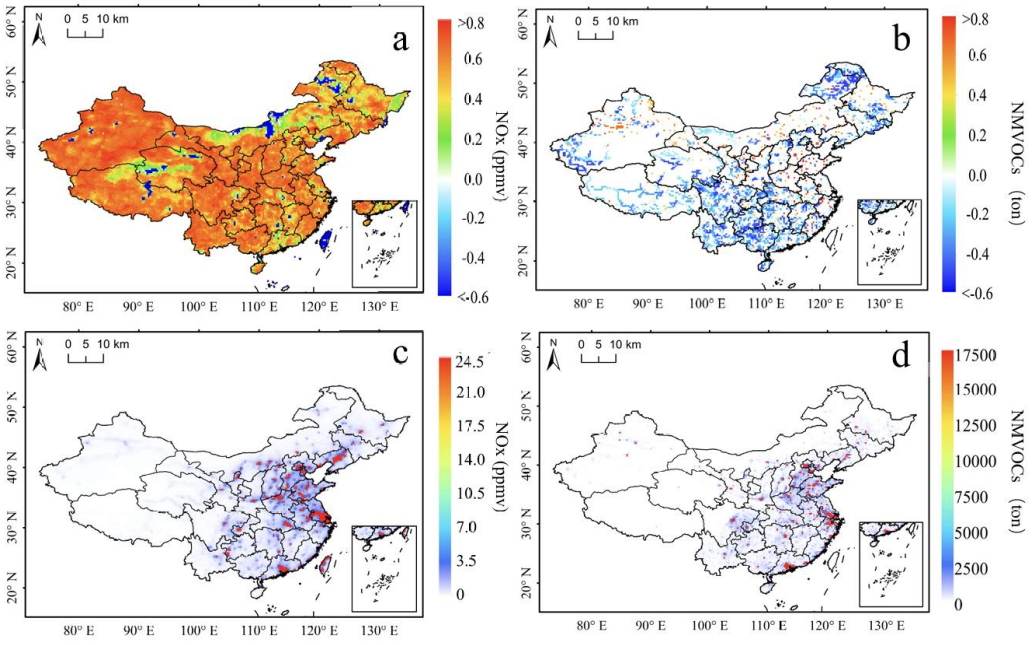

Fig. S10. NO_x (a) and NMVOC (b) emission trends in China from 1998 to 2017 estimated by the MK test, the trends are well within the statistically significant range at 95% confidence level between -1.96 and 1.96. NO_x (c) and NMVOC (d) mean emission in China averaged from 1998 to 2017.

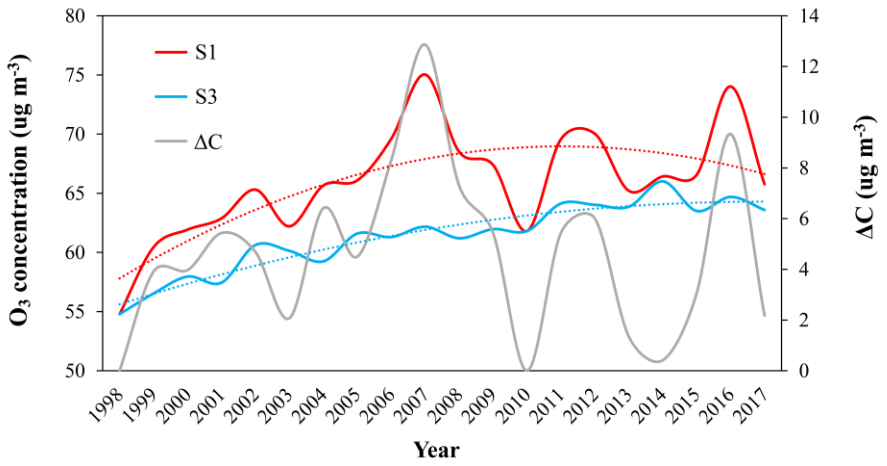

Fig. S11. Summer O_3 concentrations under S1 (red solid line, C_{S1}) and S3 (blue solid line, C_{S3}) scenarios scaled on the left-Y axis, and their difference ($\Delta C = C_{S1} - C_{S3}$, grey solid line) in Inner Mongolia scaled on the right-Y axis. The red and blue dotted lines represent the trend of O_3 concentrations under S1and S3, respectively.

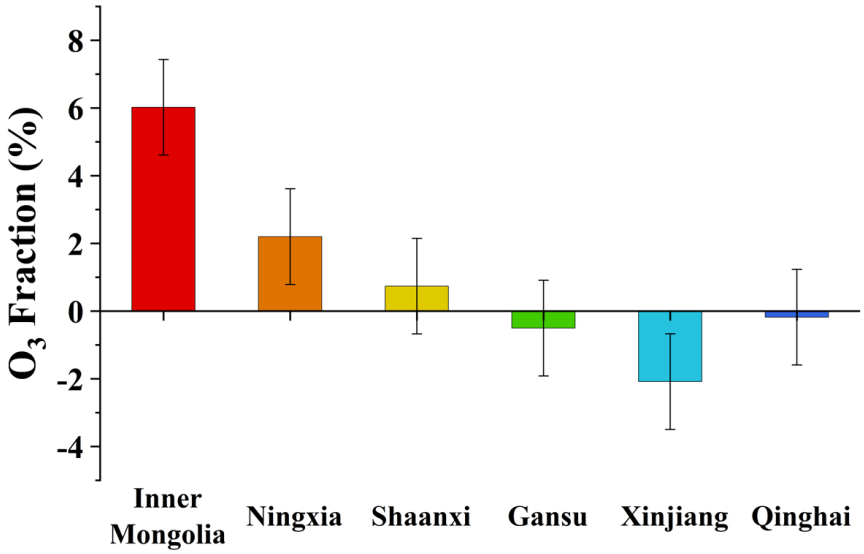

Fig. S12. O_3 attribution to meteorology between 1998 and 2017 in six provinces of NW under the S2 scenario.

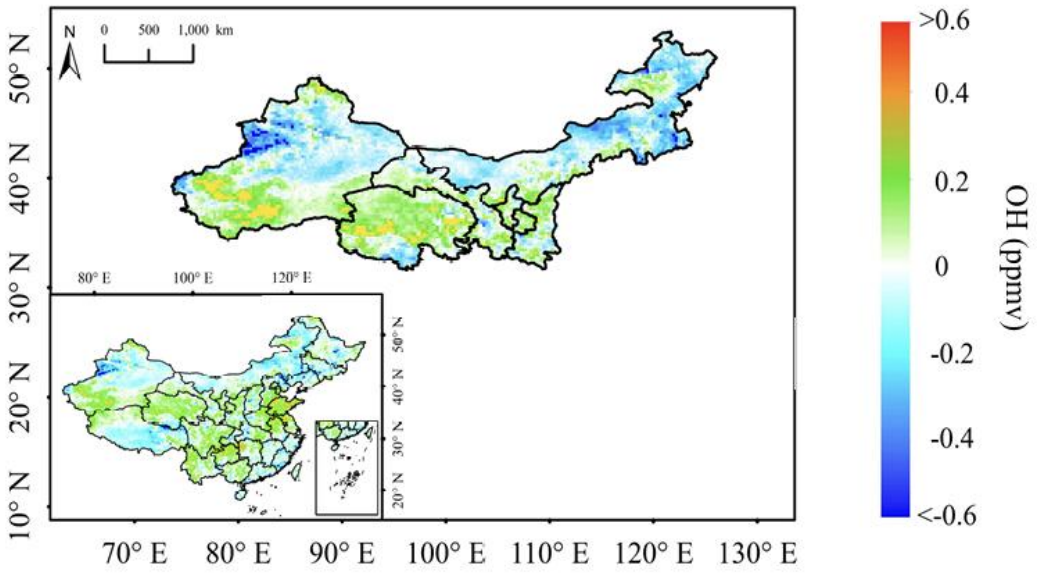

Fig. S13. Summer OH concentration trend from 1998 to 2017.

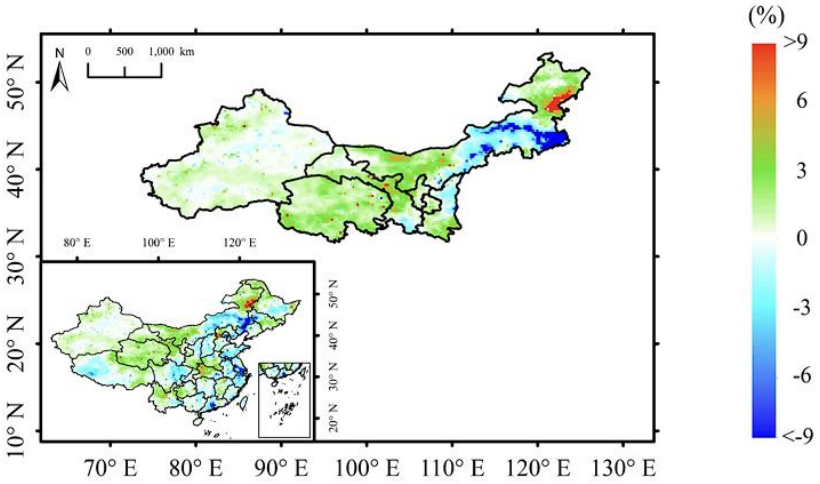

Fig. S14. WRF-Chem simulated O_3 concentration fractions between the model scenario with fixed LUC and baseline scenario S1 with varying LUC from 1998 to 2017.

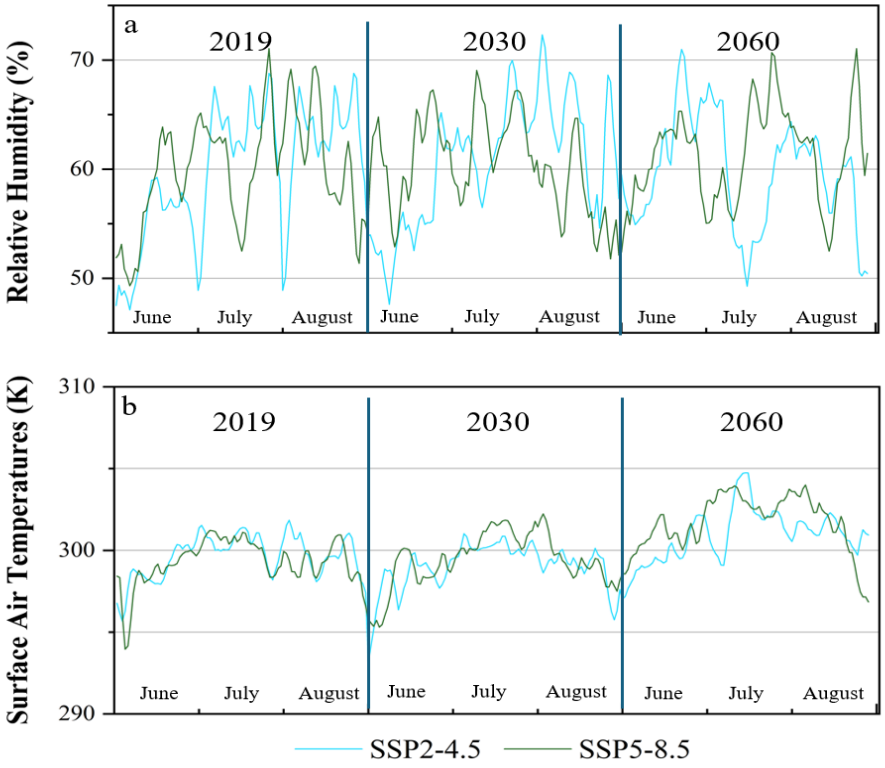

Fig. S15. Modeled RH(a) and SAT(b) time series under SSP2-4.5 and SSP 5-8.5 scenarios

References

Ackermann, I. J., Hass, H., Memmesheimer, M., Ebel, A., Binkowski, F. S., and Shankar, U.: Modal aerosol dynamics model for Europe: Development and first applications, Atmos. Environ., 32, 2981–2999, https://doi.org/10.1016/S1352-2310(98)00006-5, 1998.

Chen, F., and Dudhia, J.: Coupling an Advanced Land Surface–Hydrology Model with the Penn State–NCAR MM5 Modeling System. Part I: Model Implementation and Sensitivity, Mon. Weather Rev., 129, 569–585, https://doi.org/10.1175/1520-0493(2001)129<0569:CAALSH>2.0.CO;2, 2001.

Chou, M., Suarez, M. J., Ho, C., Yan, M., and Lee, K.: Parameterizations for Cloud Overlapping and Shortwave Single-Scattering Properties for Use in General Circulation and Cloud Ensemble Models, J. Clim., 11, 202–214, https://doi.org/10.1175/1520-0442(1998)011<0202:PFCOAS>2.0.CO;2, 1998.

Grell, G. A., and Dévényi, D.: A generalized approach to parameterizing convection combining ensemble and data assimilation techniques, Geophys. Res. Lett., 29, 38-1-38-4, https://doi.org/10.1029/2002GL015311, 2002.

Janjić, Z. I.: The Step-Mountain Eta Coordinate Model: Further Developments of the Convection, Viscous Sublayer, and Turbulence Closure Schemes, Mon. Weather Rev., 122, 927–945, https://doi.org/10.1175/1520-0493(1994)122<0927:TSMECM>2.0.CO;2, 1994.

Jiang, F., Wang, T. J., Wang, T. T., Xie, M., and Zhao, H.: Numerical modeling of a continuous photochemical pollution episode in Hong Kong using WRF-chem, Atmos. Environ., 42, 8717–8727, https://doi.org/10.1016/j.atmosenv.2008.08.034, 2008.

Jiang, F., Zhou, P., Liu, Q., Wang, T. J., Zhuang, B. L., and Wang, X. Y.: Modeling tropospheric ozone formation over East China in springtime, J. Atmos. Chem., 69, 303–319, https://doi.org/10.1007/s10874-012-9244-3, 2012.

Li, J. X., Wang, Z. X., Chen, L. L., Lian, L. L., Li, Y., Zhao, L. Y., Zhou, S., Mao, X. X., Huang, T., Gao, H., and Ma, J. M.: WRF-Chem simulations of ozone pollution and control strategy in petrochemical industrialized and heavily polluted Lanzhou City, Northwestern China, Sci. Total Environ., 737, 139835, https://doi.org/10.1016/j.scitotenv.2020.139835, 2020.

Lin, Y., Farley, R. D., and Orville, H. D.: Bulk Parameterization of the Snow Field in a Cloud Model, J. Appl. Meteorol. Clim., 22, 1065–1092, https://doi.org/10.1175/1520-0450(1983)022<1065:BPOTSF>2.0.CO;2, 1983.

Nooni, I. K., Hagan, D. F. T., Wang, G. J., Ullah, W., Lu, J., Li, S. J., Dzakpasu, M., Prempeh, N. A., and Sian, K.: Future Changes in Simulated Evapotranspiration across Continental Africa Based on CMIP6 CNRM-CM6, Int. J. Environ. Res. Public Health, 18, 6760, https://doi.org/10.3390/ijerph18136760, 2021.

Pfannerstill, E. Y., Arata, C., Zhu, Q. D., Schulze, B. C., Ward, R., Woods, R., Harkins, C., Schwantes, R. H., Seinfeld, J. H., Bucholtz, A., Cohen, R. C., and Goldstein, A. H.: Temperature-dependent emissions dominate aerosol and ozone formation in Los Angeles, Science, 384, 1324–1329, https://doi.org/10.1126/science.adg8204, 2024.

Schell, B., Ackermann, I. J., Hass, H., Binkowski, F. S., and Ebel, A.: Modeling the formation of secondary organic aerosol within a comprehensive air quality model system, J. Geophys. Res-Atmos., 106, 28275–28293, https://doi.org/10.1029/2001JD000384, 2001.

Stockwell, W. R., Middleton, P., Chang, J. S., and Tang, X.: The second generation regional acid deposition model chemical mechanism for regional air quality modeling, J. Geophys. Res-Atmos., 95, 16343–16367, https://doi.org/10.1029/JD095iD10p16343, 1990.

Xiang, S. L., Liu, J. F., Tao, W., Yi, K., Xu, J. Y., Hu, X. R., Liu, H. Z., Wang, Y. Q.,

Zhang, Y. Z., Yang, H. Z., Hu, J. Y., Wan, Y., Wang, X. J., Ma, J. M., Wang, X. L., and Tao, S.: Control of both $PM_{2.5}$ and O_3 in Beijing-Tianjin-Hebei and the surrounding areas, Atmos. Environ., 224, 117259, https://doi.org/10.1016/j.atmosenv.2020.117259, 2020.

Zhang, X. D., Du, J., Zhang, L. M., Huang, T., Gao, H., Mao, X. X., and Ma, J. M.: Impact of afforestation on surface ozone in the North China Plain during the three-decade period, Agr. Forest Meteorol., 287, 107979, https://doi.org/10.1016/j.agrformet.2020.107979, 2020.

Zhang, X. D., Jian, X. H., Zhao, Y., Liu, X. R., Chen, K. J., Wang, L. F., Tao, S., Liu, J. F., Huang, T., Gao, H., Liu, Y. J., Zhugu, R. R., and Ma, J. M.: Tropospheric Ozone Perturbations Induced by Urban Land Expansion in China from 1980 to 2017, Environ. Sci. Technol., 56, 6978–6987, https://doi.org/10.1021/acs.est.1c06664, 2022.

Zhou, G. Q., Xu, J. M., Xie, Y., Chang, L. Y., Gao, W., Gu, Y. X., and Zhou, J.: Numerical air quality forecasting over eastern China: An operational application of WRF-Chem, Atmos. Environ., 153, 94–108, https://doi.org/10.1016/j.atmosenv.2017.01.020, 2017.

Zhou, Z. L., Zhang, L. P., Chen, J., She, D. X., Wang, G. S., Zhang, Q., Xia, J., and Zhang, Y. J.: Projecting Global Drought Risk Under Various SSP-RCP Scenarios, Earth's Future, 11, e2022EF003420, https://doi.org/10.1029/2022EF003420, 2023.

Zhu, H., Jiang, Z., Li, J., Li, W., Sun, C., and Li, L.: Does CMIP6 Inspire More Confidence in Simulating Climate Extremes over China? Adv. Atmos. Sci., 37, 1119–1132, https://doi.org/10.1007/s00376-020-9289-1, 2020.